

Efficient Ray-Tracing Simulation for Near-Field Spatial Non-Stationary mmWave Massive MIMO Channel and Its Experimental Validation

Zhiqiang Yuan^{1b}, Graduate Student Member, IEEE, Jianhua Zhang^{2b}, Senior Member, IEEE, Vittorio Degli-Esposti^{3b}, Senior Member, IEEE, Yuxiang Zhang, and Wei Fan^{4b}, Senior Member, IEEE

Abstract—Massive Multiple Input Multiple Output (MIMO) at millimeter-Wave (mmWave) frequencies is envisioned as a key technology for beyond 5G communication. Accurate channel modeling is crucial for the design and evaluation of such systems. Ray-Tracing (RT) can be used to accurately simulate the propagation channel. However, state-of-the-art RT for multi-antenna systems typically employs plane-wave extension under far-field conditions, failing to capture Near-Field (NF) and Spatial non-Stationary (SnS) properties that are observed in real-world mmWave massive MIMO channel measurements. This work aims at accurate and efficient RT simulations for massive MIMO systems, with a proposed coarse-refinement strategy capable of capturing NF and SnS. The channel is simulated using RT on a few sparsely located array elements and then interpolated onto other elements using spherical/astigmatic-wave approximation and the Uniform Theory of Diffraction, thus significantly reducing simulation complexity while maintaining accuracy. The proposed strategy is demonstrated to offer almost the same simulation accuracy as the brute-force method, with a dramatic reduction in complexity through experimental validation. The significance, novelty, effectiveness, and simplicity of the proposed

framework make it highly valuable for massive MIMO channel research.

Index Terms—Massive MIMO, ray-tracing simulation, near field, spatial non-stationarity, channel sounding and modeling.

I. INTRODUCTION

MASSIVE Multiple Input Multiple Output (MIMO) is considered as an essential component of beyond 5G communication to meet the explosive data demands [1]. While reaping all the benefits of conventional MIMO technology, massive MIMO brings huge improvements in throughput, energy efficiency, multi-user service, and link reliability through the use of a large number of antennas (tens to thousands) [2], [3], [4]. Millimeter-Wave (mmWave) frequencies, on the other hand, can be perfectly paired with massive MIMO as they offer the advantages of the vast untapped spectrum and compact deployment of large antenna arrays [5]. New spatial processing techniques operating at wideband can be explored to further enhance the benefits and applications of mmWave massive MIMO [6]. All those advantages have stimulated research enthusiasm for developing mmWave massive MIMO systems in both academia and industry [1].

Accurate channel models are essential to assist the design and deployment of mmWave massive MIMO systems [7], [8], [9]. Deterministic Ray-Tracing (RT), which relies on the ray-optic approximation, can in principle simulate the wireless channel between any couple of spatial locations (for the Transmitter (Tx) and Receiver (Rx)) with high precision [10]. Traditionally, RT performs a simple point-to-point simulation to estimate the channel between the Tx and Rx, e.g. in [11]. However, this becomes unrealistic for large-scale channel realizations due to the large array apertures with inconsistent responses across elements [12]. A straightforward strategy is to employ brute-force simulation, where RT is performed for each Tx/Rx element pair of the array. However, this might become computation-prohibitive for massive MIMO systems.

Alternatively, several works have been reported in the literature to address RT simulation for multi-antenna channels. In [13], the METIS work was proposed to employ simply RT simulation for massive MIMO systems, though no results were presented. In [14], [15], and [16], efficient RT simulations were proposed for multi-antenna systems by introducing acceleration strategies such as object space partitioning, grid computing, and GPU acceleration. In [17], [18], [19], and [20],

Manuscript received 15 August 2023; revised 15 November 2023; accepted 13 January 2024. Date of publication 30 January 2024; date of current version 14 August 2024. This work was supported in part by the National Science Fund for Distinguished Young Scholars under Grant 61925102; in part by the National Natural Science Foundation of China under Grant 92167202, Grant 62201087, Grant 62101069, and Grant 62201086; in part by the Beijing University of Posts and Telecommunications (BUPT)-China Mobile Communications Corporation (CMCC) Joint Innovation Center; in part by the Start-Up Research Fund of Southeast University under Project RF1028623309; in part by the European Partnership on Metrology Project Metrology for Emerging Wireless Standards (MEWS) funded by the European Partnership on Metrology under Grant 21NRM03; and in part by the European Cooperation in Science and Technology (COST) Action INTERACT under Grant CA20120. The associate editor coordinating the review of this article and approving it for publication was J. Hamalainen. (Corresponding author: Wei Fan.)

Zhiqiang Yuan is with the State Key Laboratory of Networking and Switching Technology, Beijing University of Posts and Telecommunications (BUPT), Beijing 100876, China, and the Antennas, Propagation, and Millimeter-Wave Systems (APMS) Section, Aalborg University, 9220 Aalborg, Denmark (e-mail: yuanzhiqiang@bupt.edu.cn).

Jianhua Zhang and Yuxiang Zhang are with the State Key Laboratory of Networking and Switching Technology, Beijing University of Posts and Telecommunications (BUPT), Beijing 100876, China (e-mail: jhzhang@bupt.edu.cn; zhangyx@bupt.edu.cn).

Vittorio Degli-Esposti is with the Department of Electrical, Electronic and Information Engineering “Guglielmo Marconi,” CNIT, University of Bologna, 40126 Bologna, Italy (e-mail: v.degliesti@unibo.it).

Wei Fan is with the National Mobile Communications Research Laboratory, School of Information Science and Engineering, Southeast University, Nanjing 210096, China (e-mail: weifan@seu.edu.cn).

Color versions of one or more figures in this article are available at <https://doi.org/10.1109/TWC.2024.3357071>.

Digital Object Identifier 10.1109/TWC.2024.3357071

performance of RT simulations for MIMO and massive MIMO systems and their comparisons with measurements were analyzed. However, brute-force simulations for all element pairs were still employed in the above studies. In [21], a plane-wave extension method was proposed for RT-aided MIMO channel realization. Only one Tx-Rx element pair was simulated in RT, and channels for other element pairs were obtained by plane-wave expansion of the single-pair RT simulated result under the Far-Field (FF) assumption. This assumption is useful for MIMO radios with a small aperture. In [14] and [22], the plane-wave extension method was applied to obtain the MIMO channel, where a good agreement in terms of capacity between RT channels from the brute-force and plane-wave extension simulations was achieved. In [23], the plane-wave extension method was exploited in RT simulation for massive MIMO systems in the context of human exposure evaluation.

As discussed, the state-of-the-art plane-wave extension method is popularly adopted for MIMO systems with small-scale arrays. However, it becomes problematic for large-scale massive MIMO systems, since it fails to capture the Near-Field (NF) and Spatial non-Stationary (SnS) effects in the channel. In fact, the FF assumption, which is the foundation of the plane-wave extension, holds only when the distance between the Tx and Rx is larger than the Fraunhofer distance (i.e., $2D^2/\lambda$ where D^2 and λ denote array aperture and wavelength, respectively) [24]. Such assumption can be violated in the typical mmWave massive MIMO scenarios due to the large aperture, millimeter-lever wavelength, and small cell configuration [25], [26], [27]. The NF and SnS properties hence arise in massive MIMO systems and have been observed in several massive MIMO channel measurements, e.g., [28], [29], [30], and [31]. Specifically, elements on a large antenna array might observe a path with different angle and delay due to NF communication distance. Besides, antenna elements at different spatial positions on the large array might observe different channel multipath characteristics including the power and number of multipaths, which is so-called the SnS property. These properties have a huge impact on the channel capacity and beamforming performance of massive MIMO systems [32], and would also lead to inaccurate channel parameter estimation for current beamforming algorithms [33], which requires accurate channel modeling. In state-of-the-art studies, RT simulations including NF and SnS effects are rarely reported, and a thorough experimental validation of RT simulation for massive MIMO channels is currently lacking. The commonly used plane-wave extension method fail to model the NF SnS channel in a realistic manner and the brute-force solution may be computationally prohibitive for massive MIMO antenna arrays. An intuitive explanation of the channel NF and SnS properties and how they can be reconstructed in exiting methods is given here, with the help of Fig. 1 in Section II. As shown, the presence of the obstacle and the large array result in the NF and SnS phenomena in the channel. The plane-wave extension method extends the generated response by RT at one element to the whole array, which would fail to capture the NF and SnS properties. The brute-force method is able to reconstruct the properties by taking all different element positions into con-

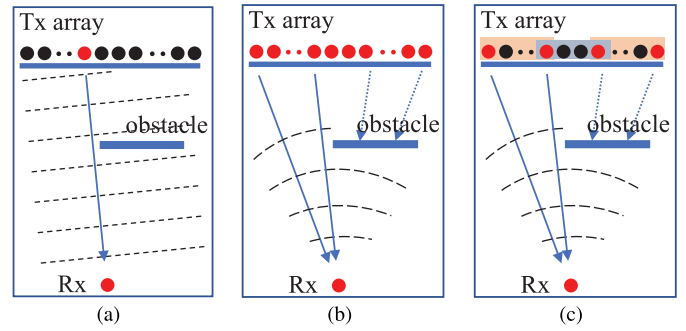


Fig. 1. Three methods used in RT simulations for massive MIMO channel realization, including (a) the plane-wave extension method, (b) the brute-force method, and (c) the coarse-refinement method. Red elements in the Tx array indicate target elements for RT simulation, while black elements indicate elements where extension is used to get the channel response. In (c), elements are divided into groups and RT calculations are performed for group ends only.

sideration. However, it suffers from unaffordable computation complexity from brute-force RT simulations, especially for massive MIMO systems. Therefore, efficient and accurate RT simulation for massive MIMO systems and the associated experimental validation remains an open research challenge.

In this work, we aim to establish an accurate and efficient deterministic RT framework for massive MIMO systems that can capture NF and SnS properties. Moreover, a massive MIMO channel measurement campaign is introduced to experimentally validate the performance of this RT framework. It is worth mentioning here that we use the same channel data and brute-force RT (as the benchmark) as in our previous work [34]. However, the research questions and objectives of the two studies are different. Reference [34] aims to build a statistical model for massive MIMO channels, while this work aims at developing an efficient and accurate RT simulation procedure based on a deterministic approach. We emphasize the contributions and novelty of this paper as follows:

- We use brute-force RT to accurately simulate NF SnS massive MIMO channels. A thorough validation with measurements is performed regarding SnS and NF properties, where numerical comparisons on path power and angles are presented. Besides, the brute-force results also serve as a reference for assessing the accuracy and complexity of the following efficient RT simulation method.
- A coarse-refinement framework is proposed for accurate and efficient RT simulation for massive MIMO systems. The basic idea is to perform RT simulations on a few sparsely located array elements and then interpolate simulated channels to the remaining elements, thus significantly reducing the simulation complexity. Besides, the proposed framework is demonstrated to achieve almost the same simulation accuracy as the brute-force method. Specifically, we implement spherical-wave and astigmatic-wave approximations with Uniform Theory of Diffraction (UTD) [35] to compensate the multipath NF propagation differences over elements, and perform “visibility judgment” on non-stationary multipaths to capture the SnS effect. To the authors’ best knowledge, it is the first time that SnS and NF effects are synthetically considered in efficient RT simulation for massive MIMO systems.

- To validate the capability of the brute-force and novel coarse-refinement methods for capturing NF and SnS effects, a massive MIMO measurement campaign is introduced as a baseline. The campaign is recently performed at 26.5-32.5 GHz in an indoor room using a large-scale (virtual) Uniform Circular Array (UCA) with 720 elements and a 1 m-diameter aperture, including one Line-of-Sight (LoS) and two Obstructed-LoS (OLOs) scenarios. Results show that the NF and SnS properties can be clearly observed in the measurements and accurately simulated by both methods.

The rest of the paper is organized as follows. In Section II, the signal model for the massive MIMO channel is first introduced. Then, the state-of-the-art plane-wave extension method, the brute force, and the proposed coarse-refinement RT simulation frameworks are discussed. Section III describes the massive MIMO channel measurement campaigns and RT simulations using the three discussed methods, and the validation results are presented in Section IV. Finally, Section V concludes this paper.

II. RT CHANNEL SIMULATION FOR MASSIVE MIMO

This section first describes the massive MIMO propagation channel with the NF and SnS properties. Then, the state-of-the-art RT channel simulation for multi-element antenna systems, namely plane-wave extension, is presented, and its incapability to model the channel NF and SnS properties is elaborated. For realistic simulation of the massive MIMO channel, a brute-force method is proposed with the NF and SnS properties accurately captured. Finally, to reduce the complexity of the brute-force method, a coarse-refinement method is proposed. It is demonstrated to efficiently reduce computation complexity with negligible accuracy degradation with respect to the brute-force method.

A. Massive MIMO Channel

Without loss of generality, we consider a propagation channel whose Tx and Rx are equipped with a P -element array and a single antenna, respectively, in this paper. Assume there are L^p multipaths transmitted by the p th Tx element at frequency f . For the l th given path ($l \in [1, L^p]$), the propagation parameters are denoted as the complex amplitude α_l^p , delay τ_l^p , azimuth and elevation angles of departure (AoD and EoD: ϕ_l^p and θ_l^p), and distance d_l^p between the element and the first-lap spherical scattering source [25]. The Channel Frequency Response (CFR) at the p th element is the superposition of L_p multipath responses,

$$H_p(f) = \sum_{l=1}^{L^p} \alpha_l^p \exp(-j2\pi f \tau_l^p). \quad (1)$$

In small radio systems, the FF plane-wave propagation channel is generally assumed. In this case, all paths are assumed to impinge on the array with the plane wavefront. Specifically, each path propagates with the same power and angle over all array elements, and the delay/phase is determined by the direction of the path and array geometry. As the

array size increases, the distance of Tx-Rx can be smaller than the Fraunhofer distance, introducing NF effects. One of the simple NF scenarios is the NF stationary case, where multipaths are assumed to propagate on the array with the NF spherical/astigmatic wavefront in the stationary mode. Each path has the wavefront-related different power, angle, and delay across array elements. Another more challenging NF scenario is the NF SnS case. As mentioned, the NF and SnS properties have been observed in massive MIMO channel measurements. Essentially, paths are assumed to propagate with the NF spherical/astigmatic wavefront, and some paths may be only visible to some of the array elements. This is mainly due to the fact that objects with limited physical sizes might not serve as complete scatterers for path propagation on such a large array. In the NF SnS massive MIMO channel, specifically, the path parameters $\{\alpha_l^p, \tau_l^p, \phi_l^p, \theta_l^p, d_l^p, L^p\}$ vary with element p , i.e., $\{\tau_l^p, \phi_l^p, \theta_l^p, d_l^p\}$ and $\{\alpha_l^p, L^p\}$ varying across p caused by the NF and SnS effects, respectively. For the realization of the massive MIMO channel, three RT methods are introduced below. Fig. 1 illustrates their basic principles.

B. State-of-the-Art: Plane-Wave Extension

In this method, the RT channel for a single Tx element and Rx pair is first simulated, and then the channels for other antenna pairs can be obtained using the plane-wave extension [22]. Fig. 1(a) illustrates the plane-wave extension method, where the channel between one Tx element (as the reference) and the Rx is first simulated by RT and then directly extended for the whole array in the form of plane waves. Mathematically, the CFR at the p th element in the extension is calculated according to (1) with the parameters as,

$$\begin{cases} \alpha_l^p = \alpha_l \\ \tau_l^p = \tau_l + \vec{v}^p \cdot \vec{\varphi}_l / c \\ \{\phi_l^p, \theta_l^p, d_l^p, L^p\} = \{\phi_l, \theta_l, d_{fr}, L\} \end{cases}, \quad (2)$$

where $\{\alpha_l, \tau_l, \phi_l, \theta_l, L\}$ are the parameters of the l th path obtained in the RT simulation for the reference point. d_{fr} denotes the Fraunhofer distance. \vec{v}^p represents the p th element's position vector, positing from the reference point to the p th element. $\vec{\varphi}_l$ is the l th path's direction vector, i.e., $\vec{\varphi}_l = [\sin \theta_l \cos \phi_l \sin \theta_l \sin \phi_l \cos \theta_l]$. c is the light speed.

However, as mentioned before, the plane-wave extension method is only applicable to small-scale multi-antenna systems under the FF assumption. It becomes problematic for simulations of the massive MIMO channel with the NF and SnS properties. For instance, in Fig. 1(a), the LoS path is directly extended with the same impinging angles and visible for the whole array in the plane-wave extension method. However, in actual propagation, the path angle significantly varies for different elements for such a large array, and the presence of the obstacle would block the path for part of the array. This phenomenon results in changes in path angles, delays, power values, and path numbers between elements. To sum up, the plane-wave extension method would fail to accurately simulate the massive MIMO channel due to the presence of the NF and SnS properties.

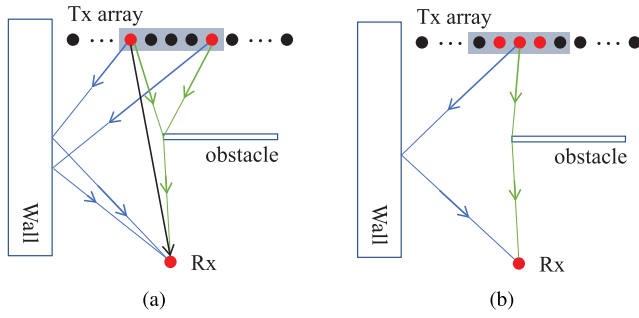


Fig. 2. Illustration of the coarse RT simulation process on a group for stationary and non-stationary paths, including (a) path generation for coarsely spaced elements (i.e. both ends) and (b) path construction for visible elements.

C. Brute-Force Method

To accurately model the NF SnS massive MIMO channel, a straightforward method is to generate the path responses on each element, i.e., via applying the brute-force strategy. Fig. 1(b) illustrates its principle, which simulates the RT channel for each array element separately. By taking different element locations and practical environment into consideration, the brute-force method can realistically characterize the NF and SnS properties of the massive MIMO channel. Note that RT simulation for massive MIMO systems using the brute-force method, though simple and straightforward, has not been adequately reported in the literature to model the NF and SnS effects of the radio channel, especially with numerical analysis and experimental validation. Besides, the brute-force strategy can be also viewed as the reference for the following efficient RT simulation method to analyze modeling accuracy and complexity.

Though capturing the massive MIMO channel well, the brute-force method suffers from the high computation cost since RT channel simulation has to be repeated for all massive MIMO elements. A strategy to reduce the computation complexity with almost the same simulation accuracy compared to the brute-force method is proposed in the following.

D. Proposed Coarse-Refinement Method

As discussed, there are two issues to be addressed in realistic massive MIMO channel realization: 1) the large physical size of the array results in the channel SnS property, i.e., the existence of non-stationary multipaths across the array; 2) the large *electrical size* (i.e. with respect to the wavelength) leads to a significant approximation error in the plane-wave extension, i.e. the NF issue. More accurate extension methods (e.g. the spherical-wave or astigmatic-wave methods) are required to characterize the channel. To accurately capture massive MIMO channels in a low complexity manner, a coarse-refinement method based on extension of coarsely simulated RT channels is proposed. Fig. 1(c) illustrates the proposed coarse-refinement method.

1) *Coarse RT Simulation*: the entire array is physically divided into several groups, and RT simulation is only performed for array elements located on both ends of the sub-arrays (or the corners for 3D arrays, see Fig. 3). Then, objects in the environment (walls, edges, etc.) are numbered and a ray is identified as the same ray over different receiving end elements through the unique list of objects it interacts

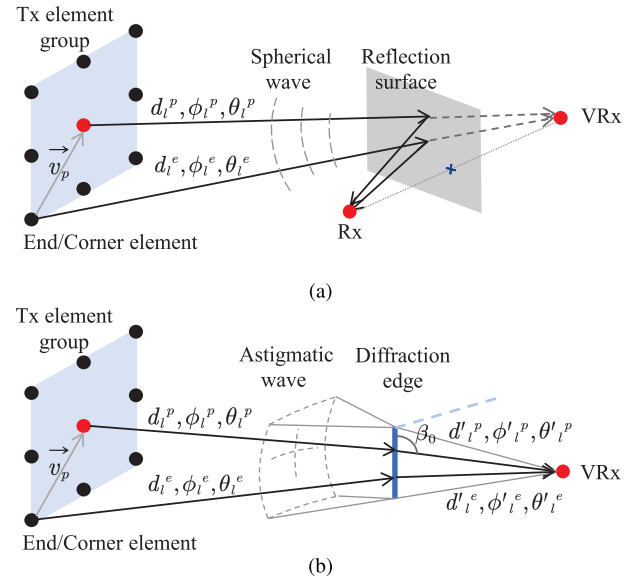


Fig. 3. Illustration of the refinement process on a group for cases of (a) LoS transmission or reflection, and (b) diffraction.

with along its path. Based on the results, multipaths can be divided into two categories, stationary and non-stationary in the group element axis, and elements visible for each path are determined:

- Stationary multipaths, i.e. paths that are present at all end/corner points in RT simulations, would be directly reconstructed for all of the other elements within the group. All group elements are “visible” for the paths.
- For non-stationary multipaths, which are not present on all end/corner points of the group, the judgment for their presence on each element would be conducted individually. Visible elements for the paths would be determined in the judgment process.

Note that the additional judgment process to determine the multipath SnS property would not significantly affect the computation complexity due to two reasons: i) There exist SnS phenomena only in few groups among the whole array, while the same multipaths will be visible across most groups due to the spatial stationary condition in small-aperture group arrays; ii) For those few groups experiencing the SnS phenomena, only few multipaths will experience it, while most paths will be stationary. Fig. 2 exemplifies the coarse simulation process. As shown, the two multipaths that are visible from both ends are directly extended to the other elements in the group, while the LoS path is determined individually for each element due to the presence of the obstacle.

2) *Refinement Process*: channel path responses for those visible elements within the group can be generated by extension of the simulated channel on group ends/corners. The path parameters (delay, angle, and complex amplitude) are calculated based on the extension of parameter values generated on the group corner according to different propagation mechanisms. Fig. 3 illustrates the refinement process. In fact, due to the image-propagation mechanism [36], paths undergoing LoS transmission or reflections will correspond to spherical waves whose center is the Rx or Rx image (i.e., virtual Rx (VRx)). Differently, since diffraction changes the shape of the wave, a path undergoing one or more diffractions will be captured

as astigmatic-wave propagation [35]. The last segment of each ray leaving the edge belongs to the Keller's cone [35], i.e. the cone forming the same angle β_0 with the edge as the incident ray segment (as shown in Fig. 3 (b)). Based on those geometry knowledge and the RT-simulated parameters of the end/corner element, the path interpolation for the group elements can be realized.

- The refinement of the LOS path or paths undergoing only reflections is illustrated in Fig. 3(a), where parameters are interpolated according to the spherical-wave propagation [37], as

$$\begin{cases} \alpha_l^p = \alpha_l^e \cdot \frac{d_l^e}{d_l^p} \\ \tau_l^p = \tau_l^e + (d_l^p - d_l^e) / c \\ \{\phi_l^p, \theta_l^p, d_l^p\} = \text{cart2sph}(\vec{d}_l^e - \vec{v}^p) \end{cases}, \quad (3)$$

where $\text{cart2sph}(\cdot)$ represents the operation that converts a vector from Cartesian to spherical coordinates, \vec{d}_l^e is the vector pointing from the end element to the spherical source as $\vec{d}_l^e = d_l^e \cdot [\sin \theta_l^e \cos \phi_l^e \sin \theta_l^e \sin \phi_l^e \cos \theta_l^e]$, and \vec{v}^p denotes the p th position vector with reference to the group end. Note that $\{\alpha_l^e, \tau_l^e, \phi_l^e, \theta_l^e, d_l^e\}$ are the path parameters obtained from the RT simulation at the group corner element, and the spherical source to calculate d_l^e in this case, i.e., LoS transmission or reflection, is defined as the Rx point or VRx (correspondingly, $d_l^e = c \cdot \tau_l^e$).

- The refinement of the path undergoing diffraction bounces is illustrated in Fig. 3(b), where path parameters are interpolated based on the astigmatic-wave propagation according to the UTD theory [35]. Note that here we only consider the case of one single diffraction at the end of the propagation chain or at its beginning (which is the same due to channel reciprocity), since mmWave communication mainly relies on dominant multipaths for data transmission, while multiple-diffracted paths are not very relevant, especially at mmWave frequencies. Mathematically, parameters are calculated as (see APPENDIX for the derivation)

$$\begin{cases} \alpha_l^p = \alpha_l^e \cdot \frac{D(\vec{d}_l^p, \vec{d}_l^e)}{D(\vec{d}_l^e, \vec{d}_l^e)} \sqrt{\frac{d_l^e d_l'^e (d_l'^e + d_l^e)}{d_l^p d_l'^p (d_l'^p + d_l^p)}} \\ \tau_l^p = \tau_l^e + (d_l^p + d_l'^p - d_l^e - d_l'^e) / c \\ \{\phi_l^p, \theta_l^p, d_l^p\} = \text{cart2sph}(\vec{d}_l^e + \vec{d}_l'^e - \vec{v}^p - \vec{d}_l'^p) \end{cases}, \quad (4)$$

where $D(\cdot, \cdot)$ denotes the diffraction coefficient related to the incidence and exit vectors representing the propagation loss during the diffraction. \vec{d}_l^p and $\vec{d}_l'^e$ are incidence vectors of the diffraction for the p th and end elements, respectively, pointing from the diffraction points to the VRx. \vec{d}_l^p and $\vec{d}_l'^e$ are the exit vectors pointing from the elements to the diffraction points in this case. Note that geometry information related to the diffraction, i.e., the position of the edge and VRx in Fig. 3(b), is required for the extension calculation (specifically, to calculate $\vec{d}_l'^p$

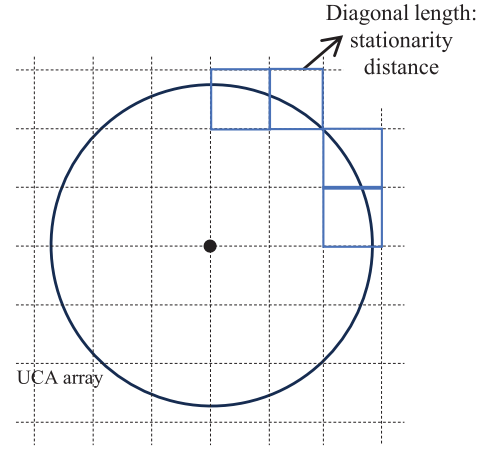


Fig. 4. An example of applying the general grouping method to a UCA. The blue squares denote the groups after division.

and $\vec{d}_l'^p$), which can be obtained from the RT simulation results at the corner elements.

Note that the proposed framework is generic to arbitrary array geometries, e.g., uniform linear array (ULA), UCA, uniform planar array (UPA), etc., and we provide a general grouping method below. The principle behind the coarse-refinement method is the spatial stationarity region assumption where most paths can be treated as stationary [38], [39], [40], according to which we can divide the array into groups and extend path responses for group elements to reduce the complexity. The spatial stationarity region is determined by the environment and has no relationship with the array geometry [38]. Usually, a distance with reference to wavelength is used to characterize the spatial stationarity region, e.g., 10 wavelengths for indoor scenarios used in [41]. Hence, for an arbitrary array, the framework can be implemented by using the line/square/cube segment with the size set according to the assumed stationarity region to divide the 1D/2D/3D array. We first set the group size, fully divide the space, and then constitute the element groups. The group size denotes the maximal distance of a segment, i.e., the length/diagonal of a line/square or cube segment. Fig. 4 illustrates the general grouping method applied to a 2D UCA as an example (which is the case in the validation).

The group physical size for dividing the array is the core parameter to be set in the coarse-refinement method, which determines the method complexity and accuracy. On the one hand, the small physical size would reduce acceleration efficiency. Specifically, with only one element in the group, the method would degrade to the brute-force strategy. On the other hand, a large group size including many array elements might reduce the modeling accuracy due to the omission of paths with birth/death behavior (i.e., multipaths that are only visible for elements in the middle of the group but not the ends/corners would be missed, or inversely). According to the spatial stationarity region assumption, it is recommended to set the group size as the stationarity region distance. Such a small size can avoid the loss of accuracy while accelerating the modeling efficiently due to the compact array distribution at mmWave bands. In the following validation, we first use the provided general grouping method with the group size set as 0.131 m/15 wavelengths to implement the framework.

and then the impact of different group sizes on accuracy and complexity is also discussed. Regarding different grouping methods, there is no significant difference in performance for a given group size. The simulation accuracy is determined by how well the introduced spherical/astigmatic-wave interpolation and non-stationary judgment can capture the wave propagation within the group region, which is not related to how elements are distributed in the region (i.e., different grouping methods).

The proposed method provides unique advantages in terms of accuracy and complexity compared to existing methods. The coarse-refinement structure can approximate the reference brute-force method with significantly reduced complexity, by relying on a few RT simulations only on a subset of selected array elements. Meanwhile, the spherical/astigmatic-wave interpolation and non-stationary judgment process are integrated into the coarse-refinement structure. It avoids the loss of accuracy by realistically capturing the near-field propagation and spatial non-stationarity. In fact, in the interpolation procedure, the default method is to linearly interpolate path parameters based on those generated at group ends. However, the simple linear interpolation method neglects the effects of the path geometry, array distribution, and non-stationarity of groups, which would suffer from accuracy degradation. Another default operation in the interpolation is to ignore the non-stationarity, i.e., treating the channel as near-field stationary channel. However, it would introduce a significant loss in accuracy for non-stationary channel realization. Those observations demonstrate the necessity of the spherical/astigmatic-wave interpolation process and the non-stationary judgment process, which carefully reconstruct the channel based on the wave propagation theory and non-stationary consideration. Note that although the principle behind the processes is complicated, their implementations would not increase much computational complexity with respect to the RT simulation. In summary, the proposed method can realize the accurate massive MIMO channel simulation with a very low complexity.

III. MEASUREMENT AND RT SIMULATION CAMPAIGNS

To validate the performance of the proposed methods for NF SnS channel realization, massive MIMO channel measurements and corresponding RT simulations using the three methods are performed. This section describes the measurement campaigns and RT simulation settings, and the next section presents the validation results. It is worth noting that the recently conducted measurement campaign was introduced in our previous work [34] for validating the developed statistical channel modeling framework. In this work, the same measurement database is used to validate the accurate and efficient deterministic RT simulation.

A. Measurement Campaign

Fig. 5 illustrates an indoor massive MIMO channel measurement campaign. The environment information, including the positions, dimensions, and materials of objects in the room, is illustrated in Fig. 5(a). As shown, a virtual UCA with a

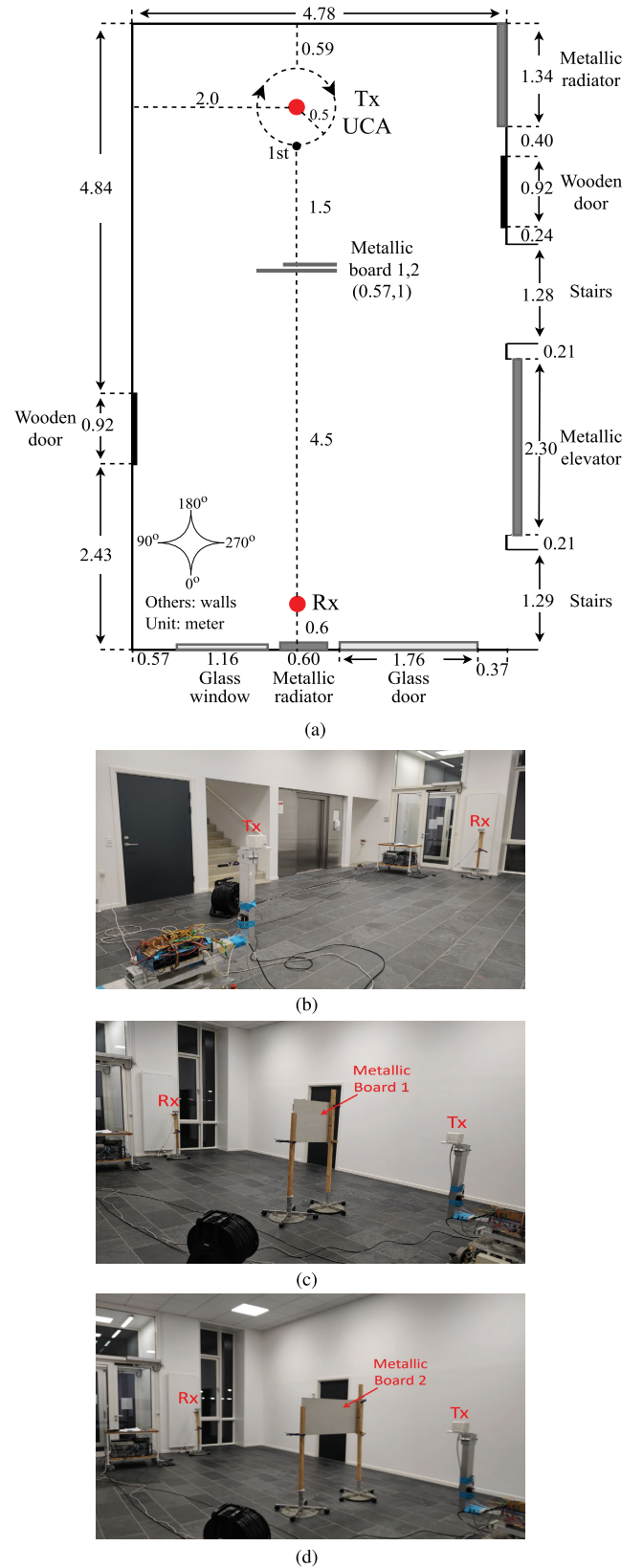


Fig. 5. Illustration of the measurement campaign, including (a) a sketch of the measurement room [34], and photos taken in the (b) LoS, (c) OLoS1, and (d) OLoS2 scenarios.

radius of 0.5 m and 720 elements is employed as the Tx and a single antenna is used as the Rx. Note that the UCA is realized by the virtual array scheme [42], where a single

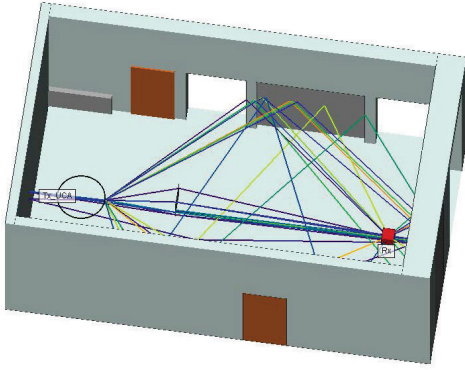


Fig. 6. The RT simulation campaign, where the three methods are performed separately in the three scenarios (i.e., LoS, OLoS1, and OLoS2).

antenna is placed off-center on a turntable and then rotated to form the array. Note that the UCA radius is selected for experimental validation according to the upper capability of the measurement system. The achievable radius is constrained to $[0, 0.5 \text{ m}]$ due to the limitation of the turntable. To mimic the massive MIMO channel, the array aperture should be set as large as possible. Besides, later measurements show that this radius setting is sufficient to capture massive MIMO channel properties. The distance between two adjacent virtual elements in the UCA is 0.0044 m . The adjacent interval is set smaller than half a wavelength to avoid spatial aliasing in signal processing. Two biconical antennas [43], [44] with vertical polarization are used for the Tx and Rx respectively. A Vector Network Analyzer (VNA) based channel sounder [45] is utilized in the measurements. The measured frequency is from 26.5 GHz to 32.5 GHz , where 1800 frequency points are swept by the VNA. To clearly observe the SnS phenomena, three scenarios, including one LoS and two OLoS scenarios, are designed in the measurements. In the LoS scenario, no metallic board is used. In the OLoS1 scenario, a metallic board with a length of 0.57 m is used to partially block the LoS path for the Tx array, while in the OLoS2 scenario, a 1 m -length metallic board is placed to completely block the LoS path for the array.

B. RT Simulations

A commercial RT software, Wireless InSite [46], which has been widely used and validated in mmWave channel research (e.g., [47]), is used in the RT simulations. As shown in Fig. 6, an indoor room with the same dimensions and objects as the real-world one is built in the simulations. Note that some objects are reconstructed with slight adjustments for simplification of the database. For example, the elevator and heating radiators that have irregular surfaces in the real world are simplified as cuboids in the simulations. Simulation configurations, including the scenarios with different boards, the Tx and Rx height, the employed array, antennas, and measured frequency, are the same as those in the measurements. The electromagnetic parameters of materials are set according to the International Telecommunication Union (ITU) recommendation [48] at 28 GHz . The path generation in RT is under the setting of 4 reflections, 1 diffraction, and 1 penetration, due to the trade-off consideration between computational complexity and modeling accuracy.

TABLE I
CONFIGURATIONS IN MEASUREMENTS & RT SIMULATIONS

Parameters	Value
Common	
Scenarios	LoS, OLoS1, OLoS2
Frequency range	$26.5\text{-}32.5 \text{ GHz}$
Frequency points	1800
Tx and Rx height	1.25 m
Radius of virtual UCA	0.5 m
Number of array elements	720
Measurements	
System	VNA-based sounder [45]
Antenna type	Biconical [43] [44]
Antenna polarization	Vertical
RT simulations	
System	Wireless InSite [46]
Antenna type	Biconical
Antenna polarization	Vertical
Material database	ITU Rec. [48]
Calculation limitation	4 ref., 1 dif., 1 pen. ⁺
Group physical size*	$0.131 \text{ m}/15\lambda$

⁺ ref.:reflection, dif.:diffraction, pen.:penetration

* Parameters for dividing the array into groups in the coarse-refinement method.

Three methods are performed in the RT simulations for each of the three scenarios (i.e., LoS, OLoS1, and OLoS2). In the plane-wave extension implementation, only one element as the reference is taken into RT calculation, and then CFRs of the entire array are generated according to (1) and (2) under the FF assumption. In the brute-force implementation, the RT calculation is repeated for each of the 720 elements to obtain the RT channels for the massive MIMO array. In the coarse-refinement implementation, the physical group size is set as 0.131 m to divide the massive MIMO array according to the recommendation as mentioned in Section II-D (other settings of the group size will be also discussed in Section IV-C). Consequently, 44 groups with common ends are divided from the array via the general grouping method. Then, 44 coarsely spaced elements (i.e., both ends of each group) are taken into the RT simulation for path generation. The refinement process for other elements based on extension of those generated paths is then performed. Finally, CFRs of all elements are generated.

As a summary, configurations in both the measurement and RT simulation campaigns are presented in Table I. In the following, results obtained in those campaigns are presented and compared for performance validation.

IV. VALIDATION RESULTS

This section presents results from massive MIMO channel measurements and RT simulations in the three scenarios. For each scenario, measured Channel Impulse Responses (CIRs, obtained by the Inverse Discrete Fourier Transformation (IDFT) of CFRs) and simulated CIRs from RT using the three methods (i.e., plane-wave extension, brute-force, and coarse-refinement) are compared. The performance of the three methods is evaluated in terms of modeling accuracy and complexity based on the result similarity and the simulation time, respectively. In addition, the impact of the group physical

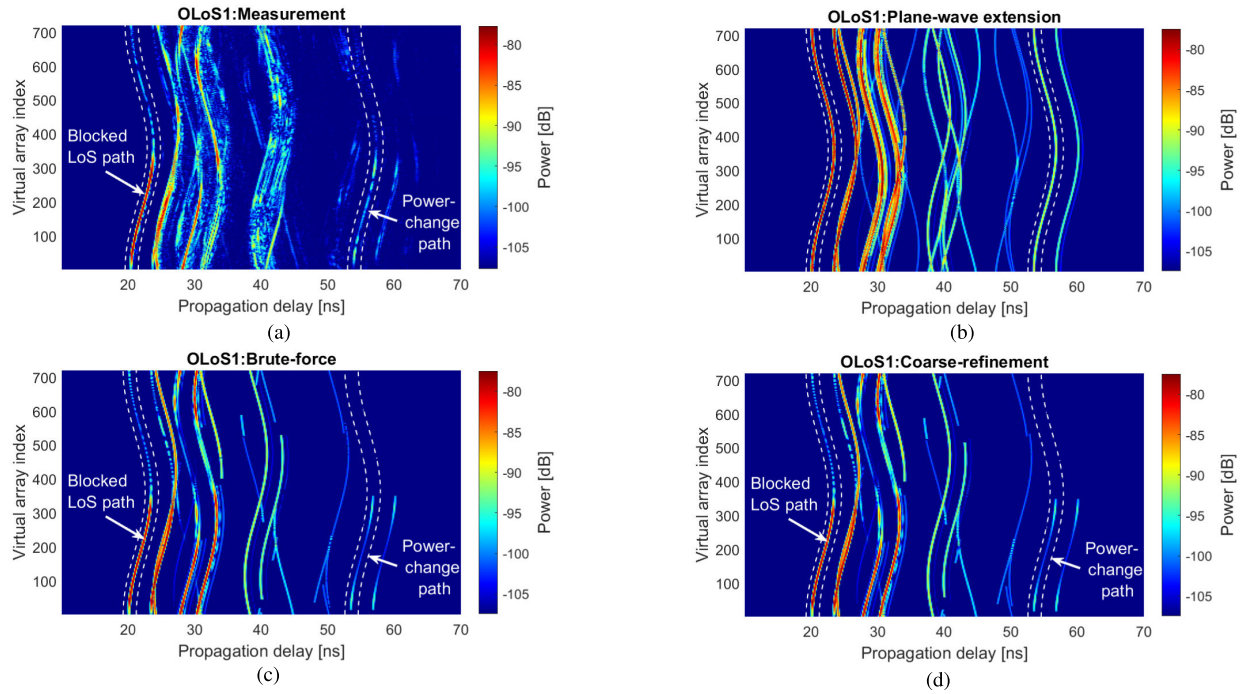


Fig. 7. CIRs across elements in the OLoS1 scenario. (a) denotes the measurement result, and (b)-(d) denote the RT simulation results with the plane-wave extension method, the brute-force method, and the coarse-refinement method, respectively. In (a), (c), and (d), two multipaths are detected with the SnS phenomena, specially marked as the blocked LoS path and power-change path. The white dashed lines in the figures confine the trajectory ranges of the two paths, where the maximum values within the ranges are calculated as the path power distributed on elements (as illustrated in Fig. 8).

size is also investigated in the implementation of the coarse-refinement methods.

A. OLoS1

Fig. 7 illustrates CIRs across elements obtained from the measurement and simulations in the OLoS1 scenario. The power dynamic range is set as 30 dB here, and also in the following LoS and OLoS2 scenarios. In the CIRs across elements, each 's'-like trajectory denotes a multipath impinging to the UCA with different delays across elements. Besides, the trajectory integrity over all elements, i.e., being complete or partial, indicates the SnS property of the path. In the measurement, i.e., Fig. 7(a), SnS phenomena can be observed for a few multipaths. For instance, two multipaths, marked as the blocked LoS path and power-change path in the figure, are visible only for part of the array due to the blockage or shadowing.¹ Besides, a significant power change across the visible elements is observed for the power-change path (see Fig. 8(b) for detailed values of the power change). Those observations show the NF and SnS properties of massive MIMO channels in actual measurements.

Fig. 7(b)-7(d) present RT-simulated CIRs across array elements by the plane-wave extension, brute-force, and the coarse-refinement method, respectively. In Fig. 7(b), all multipaths are generated with complete trajectories on the array without blockage or shadowing. It shows the plane-wave extension method fails to model the NF and SnS effects of massive MIMO channels that are present in the measurement. In Fig. 7(c), good agreement is observed by comparing with

the measured CIRs, especially for the dominant multipaths.² Besides, the channel SnS property is reconstructed well in the simulation, such as the LoS blockage and power change. Those observations demonstrate the capability of the brute-force method on NF SnS channel realization, although with high computational complexity. As shown in Fig. 7(d), the generated CIRs by the coarse-refinement method are almost identical to that of the brute-force case, with the NF and SnS properties realized as well.

Specially, we quantify the computational complexity and accuracy of the three RT methods. In our case, a brute-force simulation on 720 elements takes 649 minutes of computation on the computer with 1 Intel Xeon E5-2640 CPU, 128 GB RAM, and 4 GTX-1080Ti GPUs. On the contrary, only about 37 minutes are consumed by a coarse-refinement simulation. It indicates about 16 times acceleration efficiency is achieved by the coarse-refinement method, as around one-sixtieth of array elements (i.e., from 720 to 44) is taken into the RT simulation. In terms of accuracy, a similarity index (see (9) in [34] for details) is introduced here for evaluation. With reference to the brute-force result, the similarity of the plane-wave extension is calculated as 43.4%, and that of the coarse-refinement method is 99.6%.

Some numerical results are also presented to further assess the method performance. Fig. 8 illustrates the power distributed on elements of the two SnS paths, i.e., the blocked LoS path and power-change path. The power values are extracted from Fig. 7 (a)-(d) by selecting the maximum values

¹The LoS path is only visible for elements with indexes from about 20 to 330. In Fig. 7(a), the trajectories that have same delays yet lower power compared to the LoS path trajectory denote the diffracted paths by the board.

²It is worth mentioning that there are also some inconsistencies between measured and simulated CIRs, such as dense multipaths with delays as around 40 ns. Reasons are the lack of diffuse simulations in the RT and object simplification in the environment reconstruction as mentioned.

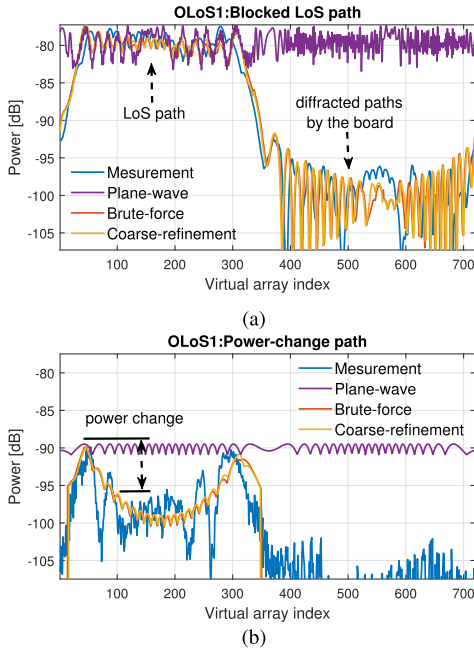


Fig. 8. Power distributed on elements of the two SnS paths, which is extracted from Fig. 7 by selecting the maximum values within the white dashed lines.

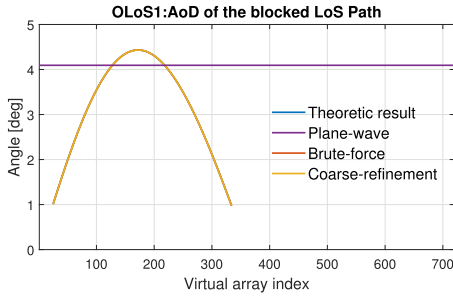


Fig. 9. Angle of Departure (AoD) of the blocked LoS path from the theoretical calculation and RT simulations with the three methods. Note that three curves from the theoretic result, brute-force method, and coarse-refinement method overlap in the figure.

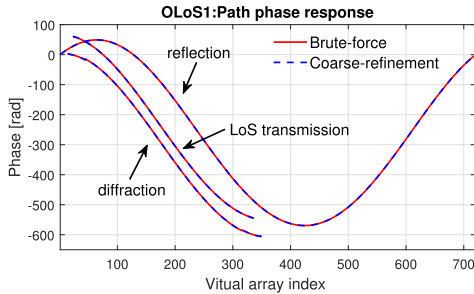


Fig. 10. Path phase responses in cases of the LoS transmission, reflection, and diffraction, calculated from the CFRs of the blocked LoS path, reflected path by the left wall (Readers can also refer to the left-wall path in Fig. 14), and power-change path in the OLoS1 scenario.

within the white dashed lines.³ The results show that the plane-wave extension method fails to capture the multipath SnS phenomena. On the contrary, the power values from the brute-force and coarse-refinement implementations agree

³Note that multipaths are generated with the same power across elements in the plane-wave extension implementation. The power variation of the blocked LoS path in the plane-wave extension case in Fig. 8(a) is mainly caused by the complex-valued superposition of the LoS path and the diffracted paths, and that of the power-change path in the plane-wave extension in Fig. 8(b) case comes from grid errors due to continuous multipath delays across elements and discrete IDFT sampling points in the delay domain.

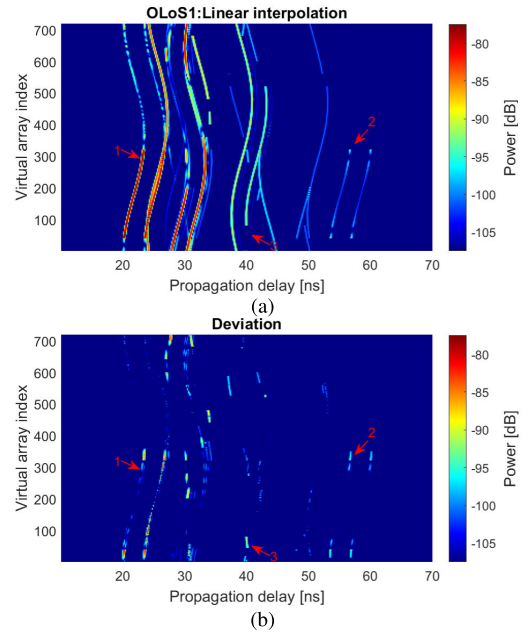


Fig. 11. Implementation of the linear interpolation in the OLoS1 scenario. (a) CIRs across elements generated by the linear interpolation, and (b) the deviation of CIRs between the brute-force result (i.e., Fig. 7(c)) and the linear interpolation result.

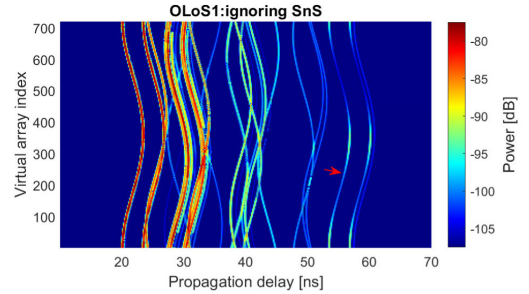


Fig. 12. Implementation of the configuration of ignoring SnS (i.e., under the NF stationary assumption) in the OLoS1 scenario.

well with that from the measurement. Furthermore, Fig. 9 presents the angle of departure (AoD) of the blocked LoS path in theory and the three RT simulations. Note that the theoretical result is calculated from the geometric location of the Tx, Rx, and metallic board. As shown, the plane-wave extension method generates the same angles for all elements. For the brute-force and coarse-refinement methods, angles changing with elements (to be exactly, element positions) are realized, which is consistent with the theoretical result. It demonstrates the characterization of the proposed method on the NF property. Moreover, Fig. 10 illustrates the path phase responses in cases of the LoS transmission, reflection, and diffraction, calculated from the phase part of the path CFRs. A good match is observed between the brute-force and coarse-refinement results for all three cases. It demonstrates the correctness of the extension principle of the proposed method. All of those results validate that the proposed method can accurately realize the NF SnS massive MIMO channel in an efficient manner.

We implement the default configurations, i.e., the linear interpolation and ignoring non-stationarity (as mentioned in Section II-D), to present a comparative analysis of the

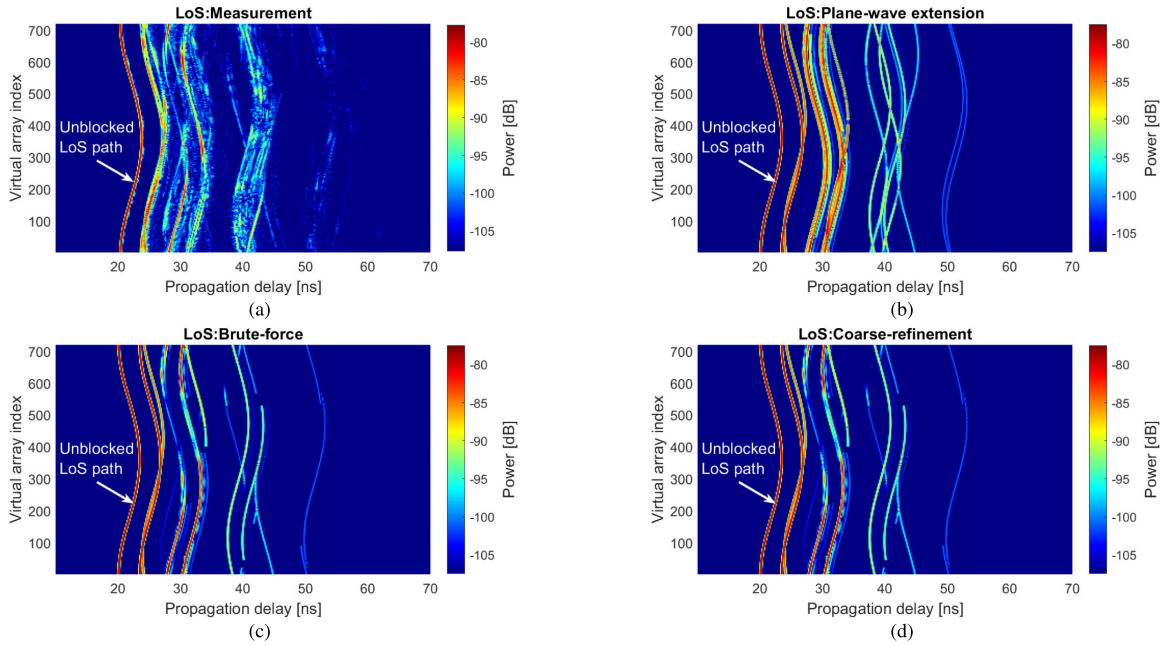


Fig. 13. CIRs across elements in the LoS scenario, obtained from (a) the measurement and RT simulations with (b) the plane-wave extension method, (c) the brute-force method, and (d) the coarse-refinement method.

proposed method. Fig. 11 shows the results of the linear interpolation in the OLoS1 scenario. It is obvious to observe the reconstruction errors with reference to the brute-force result. Three examples are marked for illustration. Mark 1 shows the parallel trajectories in the delay domain. It indicates that the linearly interpolated delays cannot simulate the actual delays. Mark 2 shows the amplitude reconstruction error with a diffracted path as an example. The mismatch comes from the fact that the phase of a diffracted path would experience a 180-degree drop (while the power is continuously distributed) on either side of the reflection boundary [49]. The linear interpolation on such two complex amplitudes would, however, lead to destructive summation due to the flipped phases. It can be concluded that linear interpolation fails to capture wave propagation in the near-field region. Mark 3 shows the disappearance of a non-stationary path response in a group. Due to lack of the path parameters at one end, one cannot generate the non-stationary path response for the group by linear interpolation. The simulation accuracy of the simple interpolation is calculated as 89.4%. Fig. 12 shows the result of ignoring non-stationarity. All paths are generated with complete trajectories via the near-field spherical/astigmatic-wave model. As marked in the figure, a diffracted path is reconstructed with power change on visible elements, which matches well with the brute-force result. However, the non-stationarity over invisible array elements is neglected, introducing a huge mismatch. The simulation accuracy of the case of ignoring non-stationarity is calculated to be 44.9%. Those results further demonstrate the necessity of the spherical/astigmatic-wave interpolation and non-stationary judgment process for accurate massive MIMO channel reconstruction.

B. LoS and OLoS2

Fig. 13 and 14 illustrate measured and simulated CIRs across elements in the LoS and OLoS2 scenarios, respectively.

By comparing the results with the measured CIRs, it can be concluded that the plane-wave extension method fails to capture the NF SnS massive MIMO channels. The realized CIRs from the brute-force method match with the measured one well, and the coarse-refinement method obtain almost the same results as the brute-force one. Besides, multipaths that are detected with the SnS property in the measurements are reconstructed in the realized CIRs by the two methods. Particularly, two multipaths are marked in the OLoS2 measurement results, i.e., Fig. 14(a), which are verified to be the first-order reflected paths from the left wall and the elevator on the right wall, respectively.⁴ The left-wall path has complete responses on the array since the left wall serves as a complete reflection scatterer for the array, while the right-wall path is detected with the partial trajectory since the elevator with limited sizes on the right wall can not act as the complete scatterer for the array. This SnS phenomenon is reconstructed well in the brute-force and coarse-refinement implementations in the OLoS2 scenario, i.e., Fig. 14(c) and 14(d).

With reference to the brute-force result, the plane-wave extension method realizes the similarity of 65.5% and 49.1%, while the coarse-refinement method achieves the similarity of 99.8% and 99.5%, in the LoS and OLoS2 scenarios, respectively. In terms of complexity, the brute-force simulations for the LoS and OLoS2 scenarios takes about 645 and 623 minutes, respectively. In the coarse-refinement cases, however, each simulation only takes about 38 minutes.

C. Analysis of Complexity and Accuracy

We analyze the complexity and accuracy of the proposed coarse-refinement method with different group sizes in the

⁴The left-wall and right-wall paths are also present in the LoS and OLoS1 scenarios and are well captured in the corresponding brute-force and coarse-refinement implementations. We take the two paths in the OLoS2 scenario as an example since they suffer less overlapping interference from other paths in the OLoS2 scenario than the other two scenarios.

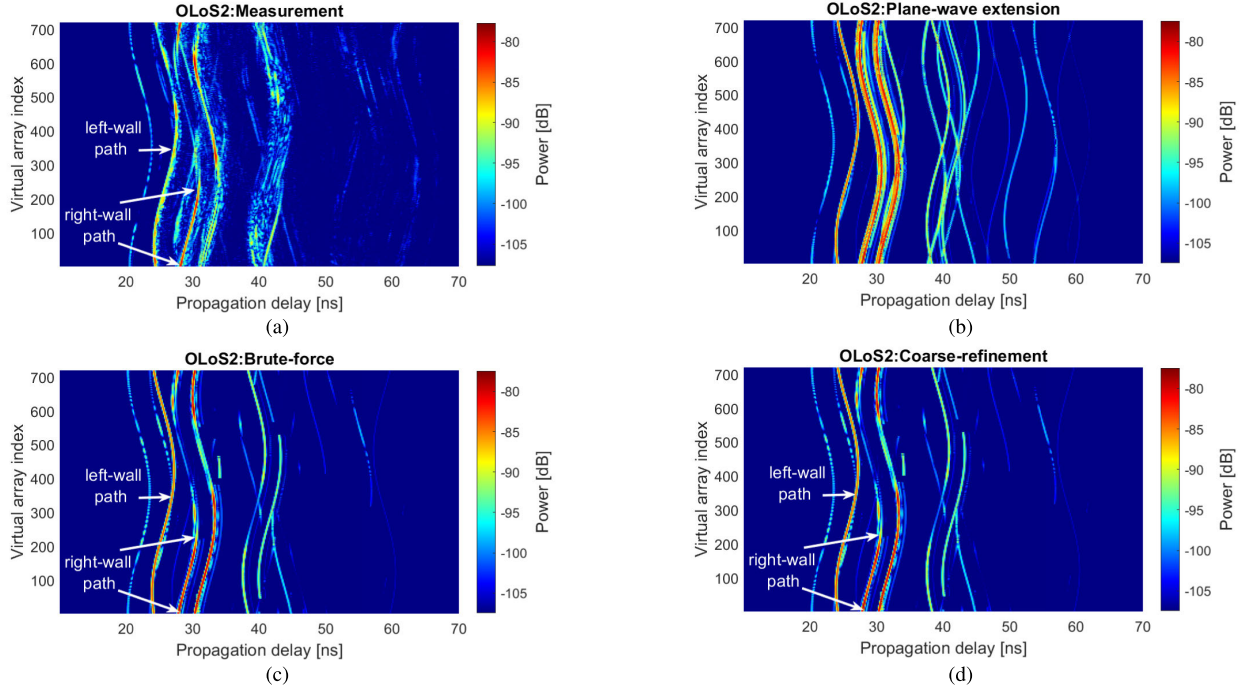


Fig. 14. CIRs across elements in the OLoS2 scenario, obtained from (a) the measurement and RT simulations with (b) the plane-wave extension method, (c) the brute-force method, and (d) the coarse-refinement method.

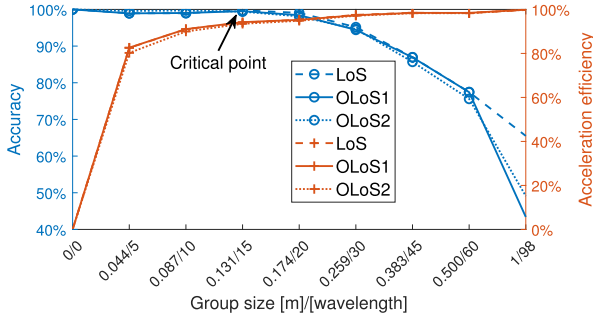


Fig. 15. Analysis of the simulation complexity (corresponding to acceleration efficiency) and accuracy of the coarse-refinement method. The cases of '0/0' and '1/98' denote the brute-force and plane-wave extension methods, respectively, serving as the references. For the brute-force method, we denote the group size as '0/0' since RT simulations are performed for each element (i.e., one element in a group). For the plane-wave extension we express the group size as '1/98' (the array aperture) since we only perform RT once (i.e., all elements are in one group). The '0.131/15' case is marked as the critical point since the accuracy starts to decrease as the group size increases.

LoS, OLoS1, and OLoS2 scenarios. For each setting of the group size, the method is implemented separately in the three scenarios, and the accuracy and acceleration efficiency are summarized in Fig. 15. The simulation accuracy denotes the similarity index calculated with reference to the brute-force result as mentioned before. The acceleration efficiency is calculated as the ratio of the saved time by the coarse-refinement simulation (compared to the brute-force method) to the brute-force simulation. Note that the greater the acceleration efficiency, the smaller the complexity will be (the sum of the two values is 1). As the group size increases, the simulation accuracy first stabilizes at around 100%, and then decreases from the case of '0.131/15'. Specifically, the accuracy values with the group size as 0.131 m are 99.8%, 99.6%, and 99.5% for the LoS, OLoS1, and OLoS2 scenarios,

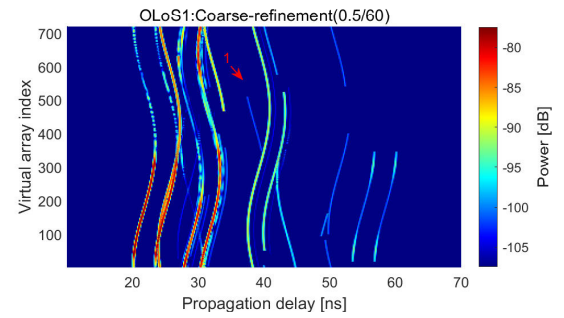


Fig. 16. CIRs obtained by the coarse-refinement method when the group size is set to '0.5/60' in the OLoS1 scenario. The mark in the figure exemplifies the omission issue under this setting.

respectively. The accuracy decrease is caused by the inaccurate approximation of the interpolation and multipath omission (see Section II-D) for such large-scale element groups. Specifically, Fig. 16 illustrates the generated CIRs by the coarse-refinement method with the group size set as '0.5/60' in the OLoS1 scenario. As shown, due to the omission of paths with death/birth behavior (as analyzed before), many mismatches with the brute-force result (i.e., Fig. 7(c)) are observed and the modeling result suffers from severe loss of accuracy. The accuracy is calculated as 76.3% in this case. An example of the omission issue is marked in the figure. Compared to the brute-force result, we observe a path that exists in the brute-force result is ignored in the modeling here. It is due to the fact that in such a large-size group (i.e. '0.5/60'), the path is only visible to middle elements but not to the end/corner elements.

On the other hand, the acceleration efficiency increases rapidly at first, and then slowly as the group size increases. Specifically, the efficiency values in the case of '0.131/15' for all three scenarios are around 94.3% (same as the 16 times acceleration efficiency as mentioned before). It indicates the

modeling process can be effectively accelerated by setting a small group size due to the compact deployment of mmWave massive MIMO arrays, with almost the same modeling accuracy guaranteed. Those results demonstrate the impact of the group size selection and validate the recommendation on setting the group size.

V. CONCLUSION

We aim to simulate RT channels for mmWave massive MIMO systems in an accurate and computationally efficient manner, focusing on capturing the NF and SnS effects of massive MIMO channels. Two methods, brute-force and novel coarse-refinement, are demonstrated and validated with mmWave massive MIMO measurements. The state-of-the-art method, i.e., plane-wave extension, fails to properly reproduce NF and SnS effects due to the violation of the far field assumption in most mmWave massive MIMO links. The brute-force method is demonstrated for accurate channel simulation but suffers from high complexity. The coarse-refinement method is based on RT simulations of a few coarsely spaced array elements to generate CIRs, and refines the other elements using the spherical/astigmatic-wave approximation and the UTD theory. It shows lower complexity and almost the same simulation accuracy compared to the brute-force method. Finally, RT simulations are performed using the mentioned three methods and corresponding massive MIMO channel measurements are performed for validation. The NF and SnS phenomena, including LoS blockage, power variation across elements, and incomplete reflection from scatterers, are clearly observed in the measurements. The plane-wave extension method cannot reconstruct those phenomena as expected while the brute-force implementation accurately realizes the NF SnS channels. The coarse-refinement method achieves around 99.5% modeling accuracy and 94.3% acceleration efficiency compared to the brute-force method for all of three measurement scenarios (one LoS and two OLoS). This work can be applied to efficient deterministic channel modeling for massive MIMO and future ultra-massive MIMO systems.

APPENDIX

Here we present the derivation of equation (4). A diffraction case is illustrated in Fig. 3(b) where the l th path impinges from the Tx element (the end element e or the group element p) to the VRx. According to the UTD [35], the received electric field E_R^e (with $E_R^e = \alpha_l^e e^{-j2\pi f \tau_l^e}$) of the diffraction ray impinging from the end element e to the VRx is calculated as,

$$E_R^e = E_T \frac{e^{-jk d_l^e}}{d_l^e} \cdot \bar{D}(\vec{d}_l^e, \vec{d}_l^e) \sqrt{\frac{d_l^e d_l^e}{d_l^e + d_l^e}} \cdot \frac{e^{-jk d_l^e}}{d_l^e}, \quad (5)$$

where $k = 2\pi/\lambda$ is propagation constant, and E_T is the emitted electric field (Note that usually the emitted electric fields for all Tx elements are normalized to be 1 to calculate propagation channel gain). $E_T \frac{e^{-jk d_l^e}}{d_l^e}$ denotes the field before the diffraction, $\bar{D}(\vec{d}_l^e, \vec{d}_l^e) \sqrt{\frac{d_l^e d_l^e}{d_l^e + d_l^e}}$ denotes the propagation loss during the diffraction, and $\frac{e^{-jk d_l^e}}{d_l^e}$ represents the field

change after the diffraction. $\bar{D}(\vec{d}_l^e, \vec{d}_l^e)$ is the diffraction coefficient, calculated according to (25) in [49]. Similarly, the received electric field E_R^p (with $E_R^p = \alpha_l^p e^{-j2\pi f \tau_l^p}$) of the diffraction ray emitted from the Tx element p with parameters $\{d_l^p, \vec{d}_l^p, d_l^p, \vec{d}_l^p\}$ (see Fig. 3(b)) is calculated as,

$$E_R^p = E_T \frac{e^{-jk d_l^p}}{d_l^p} \cdot \bar{D}(\vec{d}_l^p, \vec{d}_l^p) \sqrt{\frac{d_l^p d_l^p}{d_l^p + d_l^p}} \cdot \frac{e^{-jk d_l^p}}{d_l^p}. \quad (6)$$

The amplitude of E_R^p/E_R^e denotes the path amplitude difference between the two elements, i.e. α_l^p/α_l^e , and the phase of E_R^p/E_R^e corresponds to the path delay difference, i.e. $-j2\pi f(\tau_l^p - \tau_l^e)$. Hence, the first two terms of (4) can be derived. Besides, the path parameters of the direction for the group element p can be denoted as $\{\phi_l^p, \theta_l^p, d_l^p\} = \text{cart2sph}(\vec{d}_l^e + \vec{d}_l^e - \vec{v}^p - \vec{d}_l^p)$ according to the geometry information shown in Fig. 3(b). So far equation (4) is derived.

ACKNOWLEDGMENT

The authors would like to thank Yejian Lyu, Kim Olesen, and Kristian Henriksen Bank from Aalborg University for their assistance with the measurements.

REFERENCES

- [1] H. Tataria, M. Shafi, A. F. Molisch, M. Dohler, H. Sjöland, and F. Tufvesson, "6G wireless systems: Vision, requirements, challenges, insights, and opportunities," *Proc. IEEE*, vol. 109, no. 7, pp. 1166–1199, Jul. 2021.
- [2] E. G. Larsson, O. Edfors, F. Tufvesson, and T. L. Marzetta, "Massive MIMO for next generation wireless systems," *IEEE Commun. Mag.*, vol. 52, no. 2, pp. 186–195, Feb. 2014.
- [3] J. Zhang, Y. Zhang, Y. Yu, R. Xu, Q. Zheng, and P. Zhang, "3-D MIMO: How much does it meet our expectations observed from channel measurements?" *IEEE J. Sel. Areas Commun.*, vol. 35, no. 8, pp. 1887–1903, Aug. 2017.
- [4] F. Rusek et al., "Scaling up MIMO: Opportunities and challenges with very large arrays," *IEEE Signal Process. Mag.*, vol. 30, no. 1, pp. 40–60, Jan. 2013.
- [5] B. Ai et al., "On indoor millimeter wave massive MIMO channels: Measurement and simulation," *IEEE J. Sel. Areas Commun.*, vol. 35, no. 7, pp. 1678–1690, Jul. 2017.
- [6] S. Han, C.-L. I, Z. Xu, and C. Rowell, "Large-scale antenna systems with hybrid analog and digital beamforming for millimeter wave 5G," *IEEE Commun. Mag.*, vol. 53, no. 1, pp. 186–194, Jan. 2015.
- [7] J. Zhang, Z. Zheng, Y. Zhang, J. Xi, X. Zhao, and G. Gui, "3D MIMO for 5G NR: Several observations from 32 to massive 256 antennas based on channel measurement," *IEEE Commun. Mag.*, vol. 56, no. 3, pp. 62–70, Mar. 2018.
- [8] J.-H. Zhang, P. Tang, L. Yu, T. Jiang, and L. Tian, "Channel measurements and models for 6G: Current status and future outlook," *Frontiers Inf. Technol. Electron. Eng.*, vol. 21, no. 1, pp. 39–61, Jan. 2020.
- [9] T. S. Rappaport, Y. Xing, G. R. MacCartney, A. F. Molisch, E. Mellios, and J. Zhang, "Overview of millimeter wave communications for fifth-generation (5G) wireless networks—With a focus on propagation models," *IEEE Trans. Antennas Propag.*, vol. 65, no. 12, pp. 6213–6230, Dec. 2017.
- [10] F. Fuschini, M. Zoli, E. M. Vitucci, M. Barbiroli, and V. Degli-Esposti, "A study on millimeter-wave multiuser directional beamforming based on measurements and ray tracing simulations," *IEEE Trans. Antennas Propag.*, vol. 67, no. 4, pp. 2633–2644, Apr. 2019.
- [11] A. Karstensen, W. Fan, I. Carton, and G. F. Pedersen, "Comparison of ray tracing simulations and channel measurements at mmWave bands for indoor scenarios," in *Proc. 10th Eur. Conf. Antennas Propag. (EuCAP)*, Apr. 2016, pp. 1–5.

- [12] J. Flordelis, X. Li, O. Edfors, and F. Tufvesson, "Massive MIMO extensions to the COST 2100 channel model: Modeling and validation," *IEEE Trans. Wireless Commun.*, vol. 19, no. 1, pp. 380–394, Jan. 2020.
- [13] *METIS Channel Models*, document Deliverable/ICT-317669/D1.4 V3, Mar. 2017.
- [14] K. H. Ng, E. K. Tameh, A. Doufexi, M. Hunukumbure, and A. R. Nix, "Efficient multielement ray tracing with site-specific comparisons using measured MIMO channel data," *IEEE Trans. Veh. Technol.*, vol. 56, no. 3, pp. 1019–1032, May 2007.
- [15] G. Liu, J. She, W. Lu, M. Zhang, and Y. Bo, "3D deterministic ray tracing method for massive MIMO channel modelling and parameters extraction," *IET Commun.*, vol. 14, no. 18, pp. 3169–3174, Nov. 2020.
- [16] J. Tan, Z. Su, and Y. Long, "A full 3-D GPU-based beam-tracing method for complex indoor environments propagation modeling," *IEEE Trans. Antennas Propag.*, vol. 63, no. 6, pp. 2705–2718, Jun. 2015.
- [17] V. Degli-Esposti, V.-M. Kolmonen, E. M. Vitucci, and P. Vainikainen, "Analysis and modeling on co- and cross-polarized urban radio propagation for dual-polarized MIMO wireless systems," *IEEE Trans. Antennas Propag.*, vol. 59, no. 11, pp. 4247–4256, Nov. 2011.
- [18] J. Li et al., "On 3D cluster-based channel modeling for large-scale array communications," *IEEE Trans. Wireless Commun.*, vol. 18, no. 10, pp. 4902–4914, Oct. 2019.
- [19] C. Han, A. O. Bicen, and I. F. Akyildiz, "Multi-ray channel modeling and wideband characterization for wireless communications in the terahertz band," *IEEE Trans. Wireless Commun.*, vol. 14, no. 5, pp. 2402–2412, May 2015.
- [20] Z. Zhang et al., "Deep reinforcement learning based dynamic beam selection in dual-band communication systems," *IEEE Trans. Wireless Commun.*, early access, Aug. 7, 2023, doi: [10.1109/TWC.2023.3300830](https://doi.org/10.1109/TWC.2023.3300830).
- [21] W. Yamada, N. Kita, T. Sugiyama, and T. Nojima, "Plane-wave and vector-rotation approximation technique for reducing computational complexity to simulate MIMO propagation channel using ray-tracing," *IEICE Trans. Commun.*, vol. E92-B, no. 12, pp. 3850–3860, 2009.
- [22] S. Arikawa and Y. Karasawa, "A simplified MIMO channel characteristics evaluation scheme based on ray tracing and its application to indoor radio systems," *IEEE Antennas Wireless Propag. Lett.*, vol. 13, pp. 1737–1740, 2014.
- [23] S. Shikhantsov et al., "Hybrid ray-tracing/FDTD method for human exposure evaluation of a massive MIMO technology in an industrial indoor environment," *IEEE Access*, vol. 7, pp. 21020–21031, 2019.
- [24] S. R. Saunders and A. Aragón-Zavala, *Antennas and Propagation for Wireless Communication Systems*. Hoboken, NJ, USA: Wiley, 2007.
- [25] X. Yin, S. Wang, N. Zhang, and B. Ai, "Scatterer localization using large-scale antenna arrays based on a spherical wave-front parametric model," *IEEE Trans. Wireless Commun.*, vol. 16, no. 10, pp. 6543–6556, Oct. 2017.
- [26] R. He et al., "Characterization of quasi-stationarity regions for vehicle-to-vehicle radio channels," *IEEE Trans. Antennas Propag.*, vol. 63, no. 5, pp. 2237–2251, May 2015.
- [27] T. Jiang, J. Zhang, M. Shafi, L. Tian, and P. Tang, "The comparative study of S-V model between 3.5 and 28 GHz in indoor and outdoor scenarios," *IEEE Trans. Veh. Technol.*, vol. 69, no. 3, pp. 2351–2364, Mar. 2020.
- [28] X. Gao, F. Tufvesson, O. Edfors, and F. Rusek, "Measured propagation characteristics for very-large MIMO at 2.6 GHz," in *Proc. Conf. Rec. 46th Asilomar Conf. Signals, Syst. Comput. (ASILOMAR)*, Nov. 2012, pp. 295–299.
- [29] J. Li, B. Ai, R. He, M. Yang, Z. Zhong, and Y. Hao, "A cluster-based channel model for massive MIMO communications in indoor hotspot scenarios," *IEEE Trans. Wireless Commun.*, vol. 18, no. 8, pp. 3856–3870, Aug. 2019.
- [30] C. Wang, J. Zhang, and F. Tufvesson, "Random cluster number feature and cluster characteristics of indoor measurement at 28 GHz," *IEEE Antennas Wireless Propag. Lett.*, vol. 17, pp. 1881–1884, 2018.
- [31] X. Cai, W. Fan, X. Yin, and G. F. Pedersen, "Trajectory-aided maximum-likelihood algorithm for channel parameter estimation in ultrawideband large-scale arrays," *IEEE Trans. Antennas Propag.*, vol. 68, no. 10, pp. 7131–7143, Oct. 2020.
- [32] X. Gao, O. Edfors, F. Rusek, and F. Tufvesson, "Massive MIMO performance evaluation based on measured propagation data," *IEEE Trans. Wireless Commun.*, vol. 14, no. 7, pp. 3899–3911, Jul. 2015.
- [33] Y. Ji, W. Fan, and G. F. Pedersen, "Channel characterization for wideband large-scale antenna systems based on a low-complexity maximum likelihood estimator," *IEEE Trans. Wireless Commun.*, vol. 17, no. 9, pp. 6018–6028, Sep. 2018.
- [34] Z. Yuan, J. Zhang, Y. Ji, G. F. Pedersen, and W. Fan, "Spatial non-stationary near-field channel modeling and validation for massive MIMO systems," *IEEE Trans. Antennas Propag.*, vol. 71, no. 1, pp. 921–933, Jan. 2023.
- [35] C. A. Balanis, *Advanced Engineering Electromagnetics*. Hoboken, NJ, USA: Wiley, 1989.
- [36] H. L. Bertoni, *Radio Propagation for Modern Wireless Systems*. London, U.K.: Pearson, 1999.
- [37] K. Haneda, J.-I. Takada, and T. Kobayashi, "A parametric UWB propagation channel estimation and its performance validation in an anechoic chamber," *IEEE Trans. Microw. Theory Techn.*, vol. 54, no. 4, pp. 1802–1811, Jun. 2006.
- [38] M. Herdin, "Non-stationary indoor MIMO radio channels," Ph.D. dissertation, Technische Universität Wien, Vienna, Austria, 2004.
- [39] M. Shafi et al., "Microwave vs. millimeter-wave propagation channels: Key differences and impact on 5G cellular systems," *IEEE Commun. Mag.*, vol. 56, no. 12, pp. 14–20, Dec. 2018.
- [40] W. Sloane et al., "Analysing the 3GPP spatial consistency procedure through channel measurements," in *Proc. IEEE 32nd Annu. Int. Symp. Pers., Indoor Mobile Radio Commun. (PIMRC)*, Sep. 2021, pp. 860–865.
- [41] Qualcomm, *Channel Modeling for New Spectrum*, document 3GPP RAN Rel-19 Workshop, RWS-230173, Jun. 2023. [Online]. Available: https://www.3gpp.org/ftp/TSG_RAN/TSG_RAN/TSGR_AHs/2023_06_RAN_Rel19_WS/Docs/RWS-230173.zip
- [42] M. Dohler, F. Said, and H. Aghvami, "Concept of virtual antenna arrays," in *Proc. IEEE Globecom*, 2002, pp. 1–5.
- [43] S. S. Zhekov, A. Tatomirescu, and G. F. Pedersen, "Antenna for ultrawideband channel sounding," *IEEE Antennas Wireless Propag. Lett.*, vol. 16, pp. 692–695, 2017.
- [44] W. Fan, I. Carton, J. Ø. Nielsen, K. Olesen, and G. F. Pedersen, "Measured wideband characteristics of indoor channels at centimetric and millimetric bands," *EURASIP J. Wireless Commun. Netw.*, vol. 2016, no. 1, pp. 1–13, Dec. 2016.
- [45] Y. Lyu, A. W. Mbugua, Z. Yuan, K. Olesen, and W. Fan, "Design and validation of a multilink phase-compensated long-range ultrawideband VNA-based channel sounder," *IEEE Trans. Microw. Theory Techn.*, vol. 70, no. 10, pp. 4528–4543, Oct. 2022.
- [46] Remcom, *Wireless Insite*. Accessed: Feb. 9, 2022. [Online]. Available: <https://www.remcom.com/wireless-insite>
- [47] V. Va, J. Choi, T. Shimizu, G. Bansal, and R. W. Heath, Jr., "Inverse multipath fingerprinting for millimeter wave V2I beam alignment," *IEEE Trans. Veh. Technol.*, vol. 67, no. 5, pp. 4042–4058, May 2018.
- [48] *Effects of Building Materials and Structures on Radiowave Propagation Above About 100 MHz*, document Recommendation ITU-R P.2040-1, Jul. 2015.
- [49] R. G. Kouyoumjian and P. H. Pathak, "A uniform geometrical theory of diffraction for an edge in a perfectly conducting surface," *Proc. IEEE*, vol. 62, no. 11, pp. 1448–1461, Nov. 1974.



Zhiqiang Yuan (Graduate Student Member, IEEE) received the B.S. degree from the Beijing University of Posts and Telecommunications (BUPT) in 2018, where he is currently pursuing the Ph.D. degree. He has been a Visiting Ph.D. Student with the Antennas, Propagation, and Millimeter-Wave Systems (APMS) Section, Aalborg University, Denmark, since 2021. His current research interests include radio channel sounding and modeling for massive MIMO, mmWave, and THz systems, array signal processing, and integrated sensing and communication.



Jianhua Zhang (Senior Member, IEEE) received the Ph.D. degree in circuit and systems from BUPT in 2003. She is currently a Professor with BUPT, the Director of the BUPT-CMCC Joint Research Center, and a fellow of the China Institute of Communications. She has published more than 200 articles and authorized 50 patents. Her current research interests include beyond 5G and 6G, artificial intelligence, and data mining, especially in massive MIMO and terahertz channel modeling, channel emulators, and over-the-air (OTA) tests. She was also a member of 3GPP “5G channel model for bands up to 100 GHz.” From 2016 to 2017, she was the Drafting Group (DG) Chairperson of the ITU-R IMT-2020 (5G) channel model and led the drafting of IMT.2412 Channel Model Section. She received several paper awards, including the 2019 SCIENCE China Information Hot Paper, the 2016 China Comms Best Paper, and the 2008 JCN Best Paper. She received several prizes for her contribution to the ITU-R 4G channel model (ITU-R M.2135), the 3GPP Relay channel model (3GPP 36.814), and the 3GPP 3D channel model (3GPP 36.873). She is the Chairperson of the China IMT-2030 (6G) Tech Group—Channel Measurement and Modeling Subgroup and IEEE ComSoc Channel Modeling Subgroup.

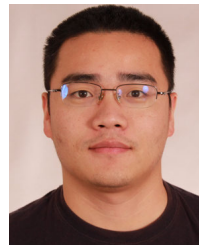


Yuxiang Zhang received the B.S. degree in electronic information engineering from the Dalian University of Technology in 2014 and the Ph.D. degree from BUPT, China, in 2020. From 2018 to 2019, he was a Visiting Scholar with the University of Waterloo. From 2020 to 2023, he was a Post-Doctoral Researcher with BUPT. He is currently an Associate Researcher with the State Key Laboratory of Networking and Switching Technology, BUPT. He has authored more than 30 papers in refereed journals and conference proceedings. His current research interests include massive/holographic MIMO, joint communication and sensing, and reconfigurable intelligent surface channel measurement and modeling.



Vittorio Degli-Esposti (Senior Member, IEEE) was the Director of Research with Polaris Wireless Inc., Mountain View, CA, USA, from January 2015 to December 2016. He was a Post-Doctoral Researcher with Polytechnic University (now the NYU Tandon School of Engineering), Brooklyn, NY, USA, in the group led by Prof. H. L. Bertoni, in 1998. He was a Visiting Professor with the Helsinki University of Technology (now Aalto University) and Tongji University, Shanghai, in 2006 and 2013, respectively. He is currently a Full Professor with

Dipartimento di Ingegneria Elettrica, Elettronica e dell'Informazione (DEI), Alma Mater Studiorum—Università di Bologna. He has participated in several European research projects, including many of the European Cooperation Actions (COST), the European Networks of Excellence NEWCOM and NEWCOM++, the Seventh Framework Program IP Project ALPHA, and the Horizon Europe Project 6G-SHINE. He has been the Co-Founder and a Lecturer of the biennial courses for Ph.D. students and researchers “Short Range Radio Propagation” and “Mobile Radio Propagation for 5G and Beyond” of the European School of Antennas (<https://www.euraap.org/esoa-courses>). He is the author or coauthor of over 160 peer-reviewed technical articles and the co-inventor of seven international patents in the fields of applied electromagnetics, radio propagation, and wireless systems. He is elected as the Chair of the Propagation Working Group of the European Association on Antennas and Propagation (EuRAAP) and of WG1 of COST Action CA20120 “Interact.” He has been the Vice-Chair of the European Conference on Antennas and Propagation (EuCAP) of the 2010 Edition and the 2011 Edition, the Short-Courses and Workshops Chair of the 2015 Edition, the Convened Sessions Chair of the 2023 Edition, an Invited Speaker at EuCAP in 2014 and the International Symposium on Antennas and Propagation (ISAP) in 2020, and the Short-Courses Chair of the European Conference on Networks and Communications (EuCNC) in 2020. He has been the Chair of the Cesena-Forlì Unit, Inter-Department Center for Industrial Research on ICT (CIRI-ICT), University of Bologna. He is an Editor of IEEE TRANSACTIONS ON VEHICULAR TECHNOLOGY and an Associate Editor of the journal *Radio Science*.



Wei Fan (Senior Member, IEEE) received the B.E. degree from the Harbin Institute of Technology, Harbin, China, in 2009, the joint master's degree (Hons.) from Politecnico di Torino, Turin, Italy, and the Grenoble Institute of Technology, Grenoble, France, in 2011, and the Ph.D. degree from Aalborg University, Aalborg, Denmark, in 2014. He was with Aalborg University, where he was an Assistant Professor in 2014, a tenured Associate Professor and a Leader of the “wireless propagation and over-the-air (OTA) testing” research group in 2017, and a

Professor (promotion program) in 2023. He was with Intel Mobile Communications, Denmark, in 2011, and with Anite Telecoms Oy (now Keysight Technologies), Finland, in 2014, as a Research Intern. He also holds a Docentship (adjunct professor) with Oulu University, Finland, since 2023. He is currently a Professor with Southeast University, China. His current research interests include OTA testing of multiple antenna systems, radio channel sounding, parameter estimation, modeling, and emulation. He is a Senior Member of AMTA and URSI and a fellow of IET. He was a recipient of the Sapere Aude Research Talent Award from the Independent Research Fund Denmark, the URSI Young Scientist Award, the IEEE AP-S Young Professional Ambassador, and the Unrestricted Research Gift Award from Meta Platforms, USA.